GDCh Research Article Angewandte International Edition Chemie www.angewandte.org

How to cite: *Angew. Chem. Int. Ed.* **2024**, e202404883
doi.org/10.1002/anie.202404883

Single-atom Catalysis

Hidden Impurities Generate False Positives in Single Atom Catalyst Imaging

Nicolò Allasia, Sean Michael Collins, Quentin Mathieu Ramasse, and Gianvito Vilé**

Abstract: Single-atom catalysts (SACs) are an emerging class of materials, leveraging maximum atom utilization and distinctive structural and electronic properties to bridge heterogeneous and homogeneous catalysis. Direct imaging methods, such as aberration-corrected high-angle annular dark-field scanning transmission electron microscopy, are commonly applied to confirm the atomic dispersion of active sites. However, interpretations of data from these techniques can be challenging due to simultaneous contributions to intensity from impurities introduced during synthesis processes, as well as any variation in position relative to the focal plane of the electron beam. To address this matter, this paper presents a comprehensive study on two representative SACs containing isolated nickel or copper atoms. Spectroscopic techniques, including X-ray absorption spectroscopy, were employed to prove the high metal dispersion of the catalytic atoms. Employing scanning transmission electron microscopy imaging combined with single-atom-sensitive electron energy loss spectroscopy, we scrutinized thin specimens of the catalysts to provide an unambiguous chemical identification of the observed single-atom species and thereby distinguish impurities from active sites at the single-atom level. Overall, the study underscores the complexity of SACs characterization and establishes the importance of the use of spectroscopy in tandem with imaging at atomic resolution to fully and reliably characterize single-atom catalysts.

Introduction

In the fields of catalysis and materials science, single-atom catalysts (SACs) have emerged as a captivating frontier, seamlessly bridging the pillars of homogeneous and heterogeneous catalysis.[1,2] These materials, composed of isolated single metal atoms stabilized on carefully-chosen supports,[3] exhibit many advantages, including enhanced activity, stability, selectivity, and recyclability.[4–6] Several studies have documented the critical role of the support materials for this category of catalysts.[7,8] Carbon nitride allotropes, including exfoliated nanosheets and mesoporous architectures,[9–11] stand out as exceptionally well-suited substrates for single-atom catalysis[12–14] due to their unique set of properties, encompassing non-toxicity, remarkable photo- and thermostability, versatile physicochemical properties, tunable surface areas, and economically viable synthesis routes from cheap and readily available precursors (e.g., melamine, cyanamide, urea).[15–17]

Commonly employed strategies for SACs synthesis include wet impregnation,[18] co-polymerization,[19] atomic layer deposition,[20,21] atom trapping,[22] pyrolysis,[23] doping,[24] ball milling,[25] adsorption approaches,[26] photoreduction,[27] galvanic replacement,[28] cyclic voltammetry,[29] ion exchange,[30,31] co-precipitation,[32] deposition-precipitation,[33] and flame spray pyrolysis.[34] However, the synthesis of SACs is not without challenges, and regardless of the chosen strategy, both metallic and non-metallic impurities of different origins can be found in the prepared materials. For example, synthesis processes involving the use of metal salts may lead to the incorporation of metallic contaminants into the final catalysts.[35] Moreover, the use of templates such as silica, employed to produce and tune the support material architecture, may result in the inclusion of non-metallic impurities, such as silicon, into the chemical composition of SACs.[36] The role of impurities in SACs is multifaceted; they may have an impact on the catalyst's structure, stability, and performance. Therefore, detecting and determining the distribution of these contaminants is essential to identify their potential sources and to develop optimization strategies for refining SACs synthesis methods aimed at producing catalysts with reduced or

[*] N. Allasia, Prof. Dr. G. Vilé
Department of Chemistry, Materials, and Chemical Engineering "Giulio Natta", Politecnico di Milano,
Piazza Leonardo da Vinci 32, 20133 Milano, Italy
E-mail: gianvito.vile@polimi.it

Dr. S. M. Collins
Bragg Centre for Materials Research, School of Chemical and Process Engineering and School of Chemistry, University of Leeds,
Woodhouse Lane, LS2 9JT Leeds, United Kingdom
E-mail: S.M.Collins@leeds.ac.uk

Dr. S. M. Collins, Prof. Dr. Q. M. Ramasse
SuperSTEM Laboratory, SciTech Daresbury Campus,
Keckwick Lane, WA4 4AD Daresbury, United Kingdom
E-mail: smcollins@superstem.org

Prof. Dr. Q. M. Ramasse
School of Chemical and Process Engineering and School of Physics,
University of Leeds,
Woodhouse Lane, LS2 9JT Leeds, United Kingdom

controlled impurity content for consistent batch-to-batch performance properties.

Critical to the SACs field is the unequivocal confirmation of the individual dispersion of active metal atoms on support materials. X-ray absorption spectroscopy (XAS), a technique enabling the measurement of the electronic properties and local coordination of SACs' individually dispersed metal active sites, is often employed to achieve this aim. While XAS is an element-selective technique, it is an ensemble measurement, meaning that the experimental spectra are a weighted average of the spectra for each constituent atomic environment for a specific chemical element: if SACs contain a metal element in multiple configurations, species, or sites, all of them will be averaged together in the recorded output spectral features.[37] Moreover, XAS can confirm single elemental dispersions, but it does not verify that all single atoms possibly present in the sample are of the type probed by XAS (given its element selectivity). Unless the types of impurities are known, or a set of candidates is established, it can be difficult to assess the elemental impurity content and/or the fraction of the sample that may be impurities from XAS. Hence, relying solely on such ensemble spectroscopies for discriminating the presence of single atoms and impurities is challenging.

Complementary to XAS, direct imaging methods are commonly applied in the form of aberration-corrected high-angle annular dark-field scanning transmission electron microscopy (HAADF-STEM).[38,39] This electron microscopy technique enables atomically resolved imaging of thin materials and shows variations in the intensity of the image (i.e., contrast) that are proportional approximately to the square of the atomic number ($\propto Z^{1.6\text{-}2}$).[40] In single-atom catalysis, HAADF-STEM has become a critical technique for confirming isolated atom dispersions, but also for evaluating whether the single atom dispersion is consistent with a random distribution (e.g., by nearest neighbor distribution analysis)[41] or exhibits clustering[42] or signatures of polynuclear conformation,[43] as well as for evaluating the areal density of single atoms.[44] In atomically-thin two-dimensional materials[45] and in well-ordered crystals,[46] HAADF-STEM imaging enables atom counting and inference of elemental distributions. However, in many practical catalytic materials with significant variations in thickness, these analyses prove challenging due to simultaneous contributions to intensity from thickness, atomic number, and any variation in position relative to the focal plane of the electron beam (i.e., defocus) which modifies the electron-sample interaction and the recorded scattering intensity. Moreover, in such materials, significant motion of atoms is observed under electron beam irradiation. While motion tracking itself can enable the extraction of surface binding energies and the character of surface binding sites,[47,48] changes in atom positions in time, and concomitant variations in defocus, further complicate intensity-based analyses of single atoms, particularly for first row transition metal-containing catalysts with a less pronounced difference in atomic number relative to common carbon- and nitrogen-based supports. Misidentification of the active single-atom sites within SACs can result in errors in the confirmation of their individual dispersion as well as derived quantities such as coverage and distribution characteristics.

In many crystalline and otherwise beam-stable materials such as graphene, a solution to the ambiguities in HAADF-STEM intensities due to thickness or compositional variations is the application of atomically-resolved spectroscopy in the form of electron energy loss spectroscopy (EELS)[49–53] or X-ray energy-dispersive spectroscopy (EDS)[54] to determine elemental composition and even electronic fine structure. Occasionally, combinations of imaging, revealing only single atoms, and spectroscopy without atomic resolution have been deployed to conclude the active species are present as single atoms.[55,56] However, the signal generated per incident electron for these spectroscopy techniques is far lower than in HAADF-STEM imaging; that is, the scattering cross-sections are 2–6 orders of magnitude lower in EELS and EDS than in HAADF-STEM imaging.[57] Consequently, longer acquisitions are required, which place even greater constraints on sample stability and atom motion in practical catalyst characterization.[58]

In this work, we report the synthesis and characterization of two carbon nitride-supported SACs containing isolated nickel or copper atoms as active metal sites. Our investigations revealed the presence of impurities in small amounts in these catalysts, which originated from the synthesis process. Several spectroscopic techniques were employed to evaluate and confirm the monoatomic dispersion of the active Ni and Cu catalytic centers within SACs structure. Leveraging direct electron detection for improved signal-to-noise STEM-EELS, we further probe atomically dispersed impurities and identify Ni and Cu single atoms, underlining the importance of atomically resolved spectroscopies as well as imaging approaches for SACs characterization.

Results and Discussion

Three catalysts—Ni_1@mpgCN_x, Cu_1@mpgCN_x, and mpgCN_x—were prepared according to an established procedure,[19] consisting of a hard template-assisted synthesis with the use of cyanamide as the building block of the carbon nitride support (for details, see the "Materials and Methods" section in the Supporting Information). In-depth investigations on the chemical nature, bond environment, and local architecture of the catalysts were afforded through a combination of spectroscopic and diffractive techniques, including attenuated total reflectance-Fourier transform infrared (ATR-FTIR) spectroscopy, X-ray diffraction (XRD), and X-ray absorption spectroscopy (XAS). The C/N ratios of the catalysts (Table 1) were found to lie in the range of 0.6–0.7, in line with data already reported in previous works for similarly synthesized carbon nitride materials.[59,60] In the literature, a certain variability among the C/N ratios has been ascribed to defects originating from the thermal polymerization process, often observable in this type of materials.[61,62] The presence of these structural imperfections can also be inferred from the detection of a low-but-not-negligible amount of hydrogen and other chem-

Table 1: Elemental composition and surface area of the synthesized metal-containing catalysts and reference support materials.

Catalyst	C[a] (wt%)	N[a] (wt%)	H[a] (wt%)	C/N (–)	Ni[b] (wt%)	Cu[b] (wt%)	Si[b] (wt%)	S_{BET}[c] ($m^2 g^{-1}$)
$mpgCN_x$	31.90	48.75	2.43	0.65	–	–	0.83	157
$Ni_1@mpgCN_x$	32.59	52.62	2.32	0.62	0.47	–	0.33	172
$Cu_1@mpgCN_x$	32.03	48.01	2.40	0.67	–	1.57	0.36	241

[a] C, N, and H content from combustion analysis. [b] ICP-OES data. [c] BET method applied on the adsorption branch of the N_2 isotherm in the $0.05 < p/p_0 < 0.3$ range.

ical species coming from the synthesis. These elements should in principle not be observed if the carbon nitride support went through complete polymerization and all the impurities were removed. Results from inductively-coupled plasma optical emission spectroscopy (ICP-OES), reported in Table 1, confirmed the successful incorporation of Ni and Cu within the porous network of the support, with a Ni loading of 0.47 wt % over $Ni_1@mpgCN_x$ and a Cu loading of 1.57 wt % over $Cu_1@mpgCN_x$. In addition, a follow-up screening of several elements via ICP-OES analysis allowed for the detection of a certain amount of Si impurities coming from the hard template employed in the SACs synthesis. In principle, Si should be removed by the action of the NH_4HF_2 etching agent employed at the end of the preparation procedure. However, some Si consistently remains in the final catalyst structure. Various durations of the etching treatment (12, 24, and 48 h) and concentrations of the NH_4HF_2 solution were tested. Contrary to expectations, prolonged etching or higher acid concentrations did not result in lower amounts of silicon impurities. A plateau was reached with etching steps longer than 24 h or NH_4HF_2 solutions exceeding 4 M, and, in both cases, impurities associated with silica persisted. While alternative etching agents like KOH can be employed for silicon removal, their use may introduce additional impurities, such as potassium species. Thus, after careful deliberation, we chose a 24 hour etching step with a 4.2 M solution of NH_4HF_2. Similarly, an increased number of washing cycles using Milli-Q® water and ethanol failed to provide any noticeable advantage in completely removing silicon impurities, which instead persisted. The significance of these impurities extends beyond mere overall quantification, and raises tantalizing questions about their structural existence, and whether these Si atoms are also erroneously identified as "single-atom catalyst" species when imaged by electron microscopy.

The surface areas of $Ni_1@mpgCN_x$, $Cu_1@mpgCN_x$, and $mpgCN_x$ were assessed via nitrogen physisorption experiments performed at −196 °C. These textural measurements yielded similar values of the BET specific surface area for all three materials (Table 1) and always larger than those typically found for bulk graphitic carbon nitride (gCN_x) or exfoliated nanosheets (nCN_x).[63] The increased surface areas shown by our materials arose from the use of a hard silica template during the synthesis procedure, which was then removed through a treatment with the NH_4HF_2 etching agent giving rise to the mesoporous structure of the supported catalysts. These results highlighted not only the porous morphology of $mpgCN_x$ with respect to the non-porous or slightly-porous network of gCN_x and nCN_x, but also how the introduction of active metal centers within the carbon nitride support did not alter the mesoporous nature of the prepared materials. These features were consistent with data previously reported in the literature.[7,19,64]

The nature of the bonding network in the CN_x support was assessed by ATR-FTIR spectroscopy. Several bands were found in the 1100–1700 cm^{-1} range of the infrared spectra (Figure 1a) and were assigned to the typical stretching modes of aromatic CN heterocycles.[65,66] The sharp peak at 805 cm^{-1} gave evidence of the characteristic breathing mode of the aromatic repeating units constituting the architecture of the CN_x support.[67,68] The broad band arising in the 3000–3500 cm^{-1} range was ascribed mainly to stretching vibrations of uncondensed primary (–NH–) and secondary ($–NH_2$) amines present in residual amino groups on the edges of CN heterocycles.[69,70] No noticeable differences were found between the infrared spectra of the $Ni_1@mpgCN_x$, $Cu_1@mpgCN_x$ SACs, and that of the metal-free support material. These observations once again demonstrated that the introduction of metal atoms into the $mpgCN_x$ framework did not induce significant chemical disruption or rearrangement of the carbon nitride bonding network or otherwise modify its formation.

Phase purity and crystallinity of $Ni_1@mpgCN_x$, $Cu_1@mpgCN_x$ and $mpgCN_x$ were evaluated by powder XRD studies. In the diffractograms reported in Figure 1b, two characteristic and broad diffraction peaks were identified at $2\theta = 13°$ and 27° and were assigned to the (100) and (002) planes of the carbon nitride system, respectively.[71,72] The former denoted the presence of the in-plane structural packing motif of aromatic units within the carbon nitride polymer, that is, the hole-to-hole distance of the pores; the latter was assigned to the interplanar stacking of CN_x layers in graphitic-like materials, i.e., the distance between the layers in the support architecture.[72] No additional peaks indexed to other phases and/or metallic clusters were observed (within the detection limit of the XRD diffractometer), suggesting the absence of other major crystalline phases such as metallic nanoparticles of considerable size. The introduction of Ni or Cu atoms within the carbon nitride framework in $Ni_1@mpgCN_x$ and $Cu_1@mpgCN_x$, respectively, was accompanied by a slight disturbance of the local CN_x network. This local structural modification was illustrated by the broadening and decrease in intensity of the stacking signal at $2\theta = 27°$ observed in the diffraction patterns of the catalysts (Figure 1b), suggesting an increased distortion of the stacking arrangement of the carbon nitride

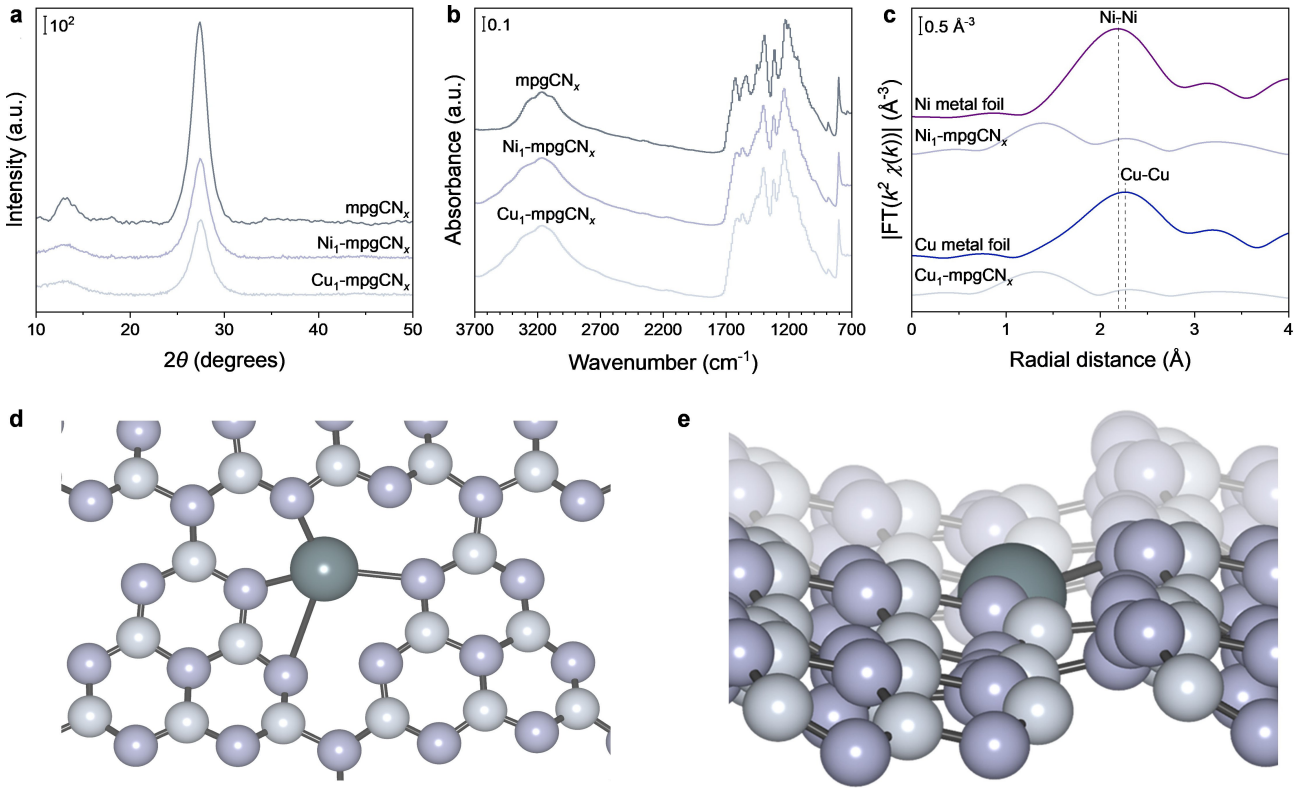

Figure 1. (a) XRD patterns and (b) ATR-FTIR spectra of Ni_1@mpgCN$_x$, Cu_1@mpgCN$_x$, and mpgCN$_x$. (c) Fourier-transform EXAFS spectra of Ni_1@mpgCN$_x$, Cu_1@mpgCN$_x$, and of the corresponding Ni and Cu reference metal foils. (d) Top view and (e) side view of a nickel atom (mineral green) hosted in the heptazinic pore of the mpgCN$_x$ support and coordinated by nitrogen atoms (smoke grey).

layers in the support material as a result of the incorporation of metal atoms in the support.[73]

Finally, XAS was applied to determine the local coordination of the monoatomic sites in the fabricated catalyst and demonstrate the absence of clusters or nanoparticles resulting from the aggregation of metal atoms.[74] In Figure 1c, the Fourier-transform extended X-ray absorption fine structure (EXAFS) spectra of the Ni_1@mpgCN$_x$ and Cu_1@mpgCN$_x$ catalysts are presented alongside those of their corresponding metal foil references. For both SACs, there was an absence of scattering contributions from metal-metal atomic pairs, which are instead observable in the corresponding metal foils.[75,76] These observations were hallmarks for the presence of Ni and Cu species as dispersed single atoms within the CN$_x$ support. The prominent peaks located at 1.30–1.50 Å in the Fourier-transform EXAFS spectra may originate from Ni–N and Cu–N first shell scattering, suggesting the coordination of Ni and Cu with nitrogen atoms in Ni_1@mpgCN$_x$ and Cu_1@mpgCN$_x$, respectively. EXAFS, however, does not allow unequivocally to determine the specific chemical elements coordinating the isolated metal atoms in a catalytic system when the former have similar atomic numbers, as in the case of carbon, oxygen, or nitrogen.[77] Nonetheless, comparisons with XAS data reported in the literature for mpgCN$_x$-supported SACs suggest that the active sites of our SACs primarily include Ni and Cu species coordinated by nitrogen atoms. Overall, all these data point consistently to the single-atom nature of our two catalysts, and to the absence of any metal clustering or aggregation in these materials. Figure 1d–e depicts the top and side view of an active nickel atom hosted in the heptazine pore of carbon nitride and coordinated by nitrogen atoms. This representation aligns with one the most frequently reported model structures of carbon nitride cavities and is supported by spectroscopic data and DFT calculations for the specific catalysts under scrutiny.[18,41,63] Therefore, the local coordination environment surrounding the active metal site in Figure 1 is merely illustrative, and alternative metal coordination arrangements can be found in the literature.[78–83]

In order to further examine the single atom dispersion by direct imaging methods, we next turned to aberration-corrected HAADF-STEM imaging. Figure 2 presents HAADF-STEM images of Ni_1@mpgCN$_x$ and Cu_1@mpgCN$_x$ acquired using an electron beam energy of 60 keV and a 36 µs per-pixel dwell time. While carbon nitrides exhibit radiolytic damage under electron beam exposure, atom movements directly arising from collisions with the incident electron beam are expected to be reduced at lower beam energies, motivating the use of 60 keV in these experiments. In this case, numerous single atoms were well-resolved as bright spots. Some 'tearing' of a number of atomic features was visible, typical of some residual atom motion during imaging and damage to the carrier support. Under these imaging conditions, sequential images on the same areas showed only minor changes to the support, with motion

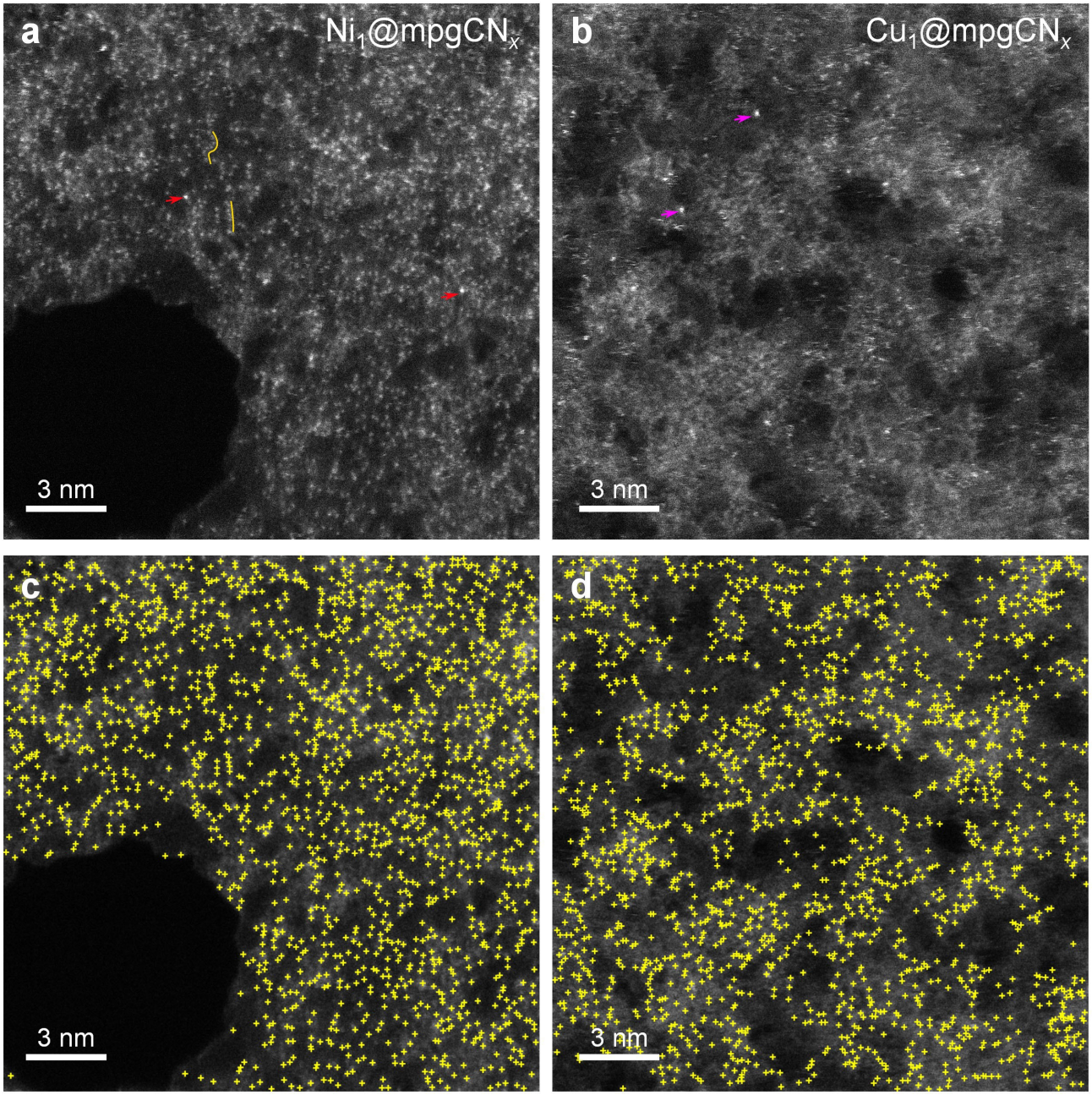

Figure 2. Single-frame HAADF-STEM images (a, b) (36 µs pixel dwell time) of (a) Ni_1@mpgCN_x and (b) Cu_1@mpgCN_x. Arrows mark atoms that appear brighter, color-coded red for Ni_1@mpgCN_x and magenta for Cu_1@mpgCN_x. Yellow lines highlight chain-like structures. Processed HAADF-STEM images (c, d) of the respective (c) Ni_1@mpgCN_x and (d) Cu_1@mpgCN_x with the single atoms automatically tagged through machine learning highlighted with yellow "+". Note that not all the tagged atoms will be correctly indexed as active metal single atom after coupling microscopy with spectroscopy (see below).

predominantly attributed to single atoms dispersed on the support (Figure S1). The support itself seemed to have some slowly varying intensity, likely due to thickness variations, which appeared to follow the mesoporosity expected from the templated synthesis.

Three key observations were drawn from these and numerous similar HAADF-STEM images of Ni_1@mpgCN_x and Cu_1@mpgCN_x: (1) Some atoms appeared brighter than other atoms distinguishable from the carbon nitride support (Figure 2, arrow markers); (2) many of the dimmer atom features exhibited chain-like ordering or clustering (Figure 2, yellow lines); (3) the overall areal density of the resolved single atoms appeared to be high considering the low metal-loadings as determined from ICP-OES (Table 1). Together, these observations raised the possibility that the images contained not only the targeted Ni or Cu single atom dispersions, but also additional impurity species dispersed as isolated atoms or clusters. We noted that some intensity

variations in SACs images were expected due to variations in thickness of the support, differences in defocus, or partial intensities due to atom jumps mid-scan. The latter effect can also produce duplicate images of atoms as the scan proceeds from the top of the frame to the bottom, so where an atom moves to a lower section of the frame, it may be imaged again. However, repeated imaging of the same area (Figure S1) ruled out many of these explanations as the atoms with differences in intensity were preserved between frames.

To evaluate unambiguously the elemental composition of the single atom dispersions, we turned to STEM-EELS. We established the hypothesis that the brightest atoms were the most likely species to be the Ni or Cu atoms. To test this hypothesis, we first examined EELS at isolated bright atom features by acquiring a single spectrum while continuously scanning an approximately 1×1 nm area around an isolated bright atom in the Ni_1@mpgCN$_x$ sample. This approach enables high quality spectra from isolated atoms, a technique established for spectroscopy of single atoms on graphene.[49,84] The continuously scanned area was of nanometer dimensions to accommodate jumps in the atom position under electron beam irradiation without loss of the atom from the field of view. Figure 3a illustrates a HAADF-STEM image averaged from a series of frames collected during the single EELS acquisition, with two energy loss ranges extracted from the single spectrum in Figure 3b–c. A single bright atom feature is visible in the HAADF-STEM image, with some dimmer atoms visible in the vicinity. All atoms exhibited significant motion, and the continuously scanning HAADF-STEM window was manually adjusted in the acquisition software to track the bright atom. As such, the consistent contribution to the signal in this setup came from the support and the bright atom feature. Figure 3b shows the C *K* and N *K* ionization edges, confirming the support's expected composition. Only a very weak signal at the O *K* edge (530 eV) was observed (see also Figure S2), commensurate with oxygen-containing impurities from the synthesis and support/sample handling. At higher energy loss values corresponding to the Ni L_{23} ionization edge (Figure 3c), we further identified an abrupt onset. After background subtracting by fitting to the pre-edge window, we recovered the characteristic Ni L_{23} edge fine structure. Noise in the single atom spectrum precluded detailed fine structure analysis, but the shape of the edge showed the characteristic bright 'white line' peak for the Ni L_{23} edge in EELS. A further example of a second acquisition on a different isolated bright atom is shown in Figure S3. These isolated atom spectra confirmed the presence of Ni single atoms on the material. However, due to the contributions of surrounding dimmer atom dispersions, the result remained not entirely unambiguous in identifying each atom type.

To move from STEM-EELS of isolated atoms to an approach for identifying atoms within an image, we turned to spectrum imaging. In STEM-EELS spectrum imaging, spectra are acquired at every position in a two-dimensional scan. Figure 4 presents results from STEM-EELS spectrum imaging of both Ni_1@mpgCN$_x$ and Cu_1@mpgCN$_x$. To obtain sufficient signal at each probe position in the scan, a much longer per-pixel dwell time and reduced pixel samples was required in comparison to HAADF-STEM imaging. Here, whereas 36 µs per-pixel dwell times were used for HAADF-STEM imaging (0.0195 nm/pixel), 10 ms per-pixel dwell times were adopted for STEM-EELS spectrum imaging (0.05 nm/pixel). Consequently, atom motion introduced greater distortion of atomic-scale features. These settings were selected to provide a balance of field of view, image resolution and limited atom motion, and EELS signal at the Ni and Cu L_{23} ionization edges. Figure 4a and Figure 4f show the HAADF-STEM images acquired simultaneously with the EELS spectrum image data for Ni_1@mpgCN$_x$ and Cu_1@mpgCN$_x$, respectively. Although these images display some streaking in the "fast-scan" direction (left-to-right) and mis-alignment of intensity in sequential rows in the "slow-scan" direction (top-to-bottom) as a result of atom motion, single atoms remain visible.

In order to examine the Ni and Cu L_{23} ionization edges, we calculated a jump ratio, that is, a (ratio of signals integrated in energy loss ranges after and before the edge onset). These images, filtered to enhance the visibility of atomic-scale features, are shown in overlay on the HAADF-

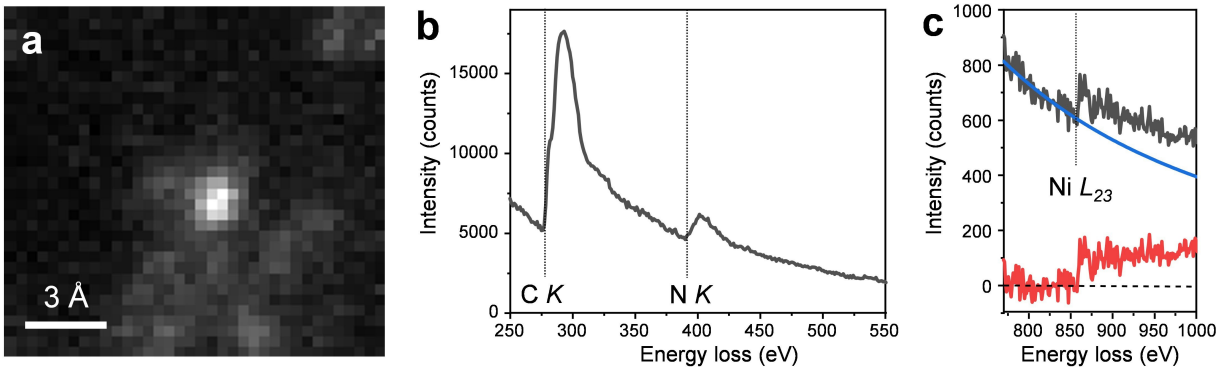

Figure 3. Spectroscopy acquired at a single Ni atom. (a) Average of 12 consecutive frames from a multi-frame HAADF-STEM series (6 µs per-pixel dwell time in each 36×33 pixel frame) of a single bright atom in Ni_1@mpgCN$_x$. A single EEL spectrum was acquired simultaneously covering (b) the C *K* and N *K* and (c) the Ni L_{23} core ionization edges. In (c) the blue line shows a power-law fit to the pre-edge background and the red trace shows the edge after background removal (stripped edge).

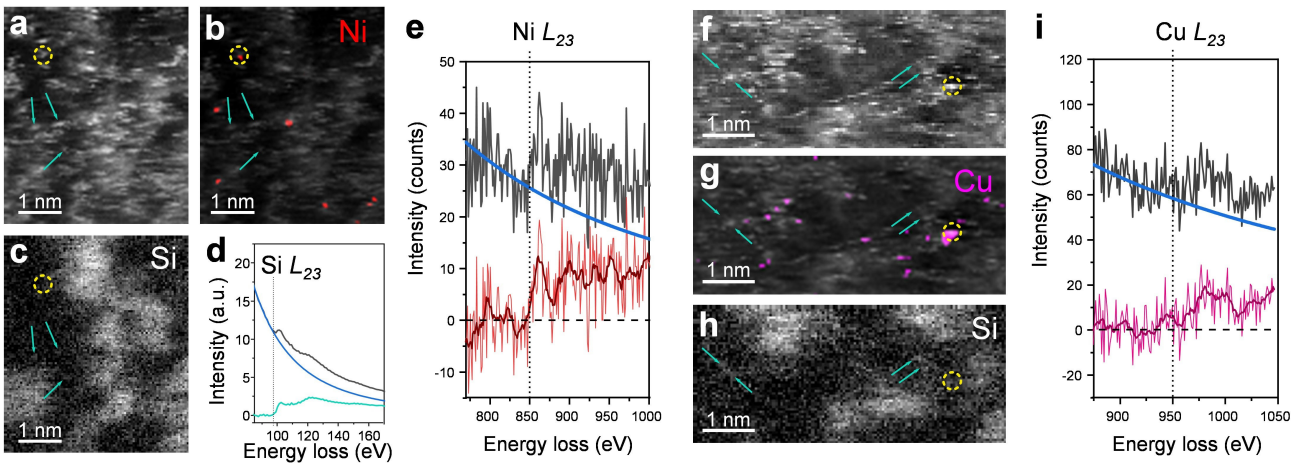

Figure 4. EELS spectrum imaging approach for the identification of Ni_1 and Cu_1 species. (a) HAADF-STEM image acquired simultaneously with EEL spectra at each pixel on Ni_1@mpgCN$_x$. (b) Overlaid HAADF-STEM image and a map of Ni distribution, taken as the jump ratio at the Ni L_{23} edge and filtered with a two-dimensional Gaussian kernel to improve visibility of atomic features. (c) EELS map at the Si L_{23} edge, produced by integrating the edge after background subtraction. (d) An example of the Si L_{23} edge and background removal from the sum spectrum integrated across the field of view shown. (e) Ni L_{23} spectrum from the marked atom (yellow dashed circle in (a–c)). The solid line shows a moving average as a guide to the eye. (f) HAADF-STEM image acquired with an EELS spectrum image on Cu_1@mpgCN$_x$. (g) Overlay of the HAADF-STEM image and a map of Cu distribution. (h) The corresponding Si EELS map. (i) Cu L_{23} spectrum from the marked atom (yellow dashed circle in (f–h)). The solid line shows a moving average as a guide to the eye. Cyan arrows mark atomic features resolved in the Si L_{23} map, also overlaid on corresponding HAADF-STEM images.

STEM images in Figure 4b and Figure 4g for Ni_1@mpgCN$_x$ and Cu_1@mpgCN$_x$, respectively, and highlight the most probable locations of Ni and Cu species. A complete set of HAADF-STEM images, Ni and Cu EELS maps, and EELS maps overlayed with the HAADF-STEM images can be found in Figure S4 and S5, respectively. To verify this speciation, we then extracted EEL spectra from selected positions identified as Ni and Cu atoms. Figure 4e and Figure 4i show Ni L_{23} and Cu L_{23} edge spectra extracted from individual atomic positions visible in the HAADF-STEM and jump ratio maps for Ni_1@mpgCN$_x$ and Cu_1@mpgCN$_x$, respectively. The spectra are noisy, as they were acquired at or near the limit of detection due to the compromise in EELS acquisition time and dwell times in STEM for preserving atomically-resolved imaging conditions. However, pronounced and abrupt onsets were detected in the spectra before processing for background removal. The Ni L_{23} spectrum shows some indications of the white line structure expected of metallic Ni; notably, the metallic Cu L_{23} edge is not expected to show a bright feature as its full *d*-orbital bands do not offer discrete transition energies above the Fermi energy. Additional examples of extracted EEL spectra related to Ni and Cu atoms are reported in Figures S6–S7.

We acquired a substantial energy loss range in these experiments, covering 0 eV to >1000 eV energy loss in the STEM-EELS spectrum images. This range enabled a broad-spectrum assessment of impurities. A pronounced feature was detected at approximately 100 eV energy loss, in addition to the C *K* and N *K* edges observed in Figure 3. This feature corresponds to the Si L_{23} edge, indicating a significant contribution from Si impurities within these catalysts. Given the minimal quantities of oxygen detected via EELS, it became evident that, while the formation of Si–O groups (e.g., silanols) may occur, these silicon impurities appeared more likely dispersed or adsorbed within the CN_x matrix, rather than forming silicon oxide particles. We also did not see any evidence of silicon interactions with nickel or copper centers, as indicated by the absence of Ni–Si and Cu–Si scattering contributions in the EXAFS spectra. Therefore, as the samples showed only single atom dispersions and an unresolved carbon nitride support in the background of the image, we identified Si as present as dispersed Si atoms on the carbon nitride support. By background subtracting and integrating the Si L_{23} edge in the STEM-EELS spectrum images, we obtained the Si elemental distribution maps displayed in Figure 4c and Figure 4h for Ni_1@mpgCN$_x$ and Cu_1@mpgCN$_x$, respectively. Figure 4d shows an example of this energy range and the background removal process for a spectrum integrated across the entire field of view analyzed for Ni_1@mpgCN$_x$ sample. The spatial distribution of the Si intensity aligned with numerous single atoms visible in the HAADF-STEM image, and several isolated atomic-scale features were also observed in the Si maps (cyan arrows, Figure 4), indicating Si single atom dispersions.

Notably, several of the identified Ni and Cu single atoms showed no overlap with regions of high intensity in the Si map (yellow dashed circles, Figure 4), further confirming separation of the Ni and Cu species from Si impurities. Not all single atoms visible in the HAADF-STEM were unequivocally assigned to either Ni, Cu, or Si. This constraint may point to additional impurities not detected or to some atomic motion precluding accumulation of sufficient EELS signal for atom identification at these positions. While motion may remove signal in EELS, the HAADF-STEM

image may still record sufficient signal-to-noise from these positions to capture an atomic feature, given the far lower dwell time required to form sufficient signal in HAADF-STEM. This difference arises from the fundamental scattering physics, with the scattering cross-section for HAADF-STEM established as 2–3 orders of magnitude greater than the scattering cross-sections for EELS.[57] The greater apparent blurring in the Si maps was likely due to their higher areal density, although greater motion for lighter species was also expected under electron beam irradiation. Similar blurring appeared in averaging of repeated HAADF-STEM images (Figure S1), indicating likely blurring of dimmer Si atom features due to motion during image acquisition.

The positively identified Ni and Cu atoms did appear to be generally brighter features in HAADF-STEM images and the major impurities appeared to be Si atoms, further corroborating the interpretation of EELS of isolated atoms in Figure 3. Together, these STEM-EELS observations elucidated the presence and atomically-dispersed characteristics of Si impurities in Ni_1@mpgCN$_x$ and Cu_1@mpgCN$_x$, and they further highlighted the risks of misidentification of dispersed single atom species by HAADF-STEM imaging alone as well as the importance of complementing any speciation analysis with single-atom sensitive spectroscopic information.

Not all single-atom catalyst metals, however, will offer EELS edges that are amenable to the STEM-EELS spectrum imaging approach. Since heavier atoms may be more readily distinguished by their atomic number contrast, we have further considered whether intensity analysis in HAADF-STEM could extend the STEM-EELS measurement. STEM-EDS of single atoms[54] may offer an alternative to EELS for some elements, though recorded EDS signals are generally weaker (lower experimental scattering cross-sections)[57] and do not generally offer any degree of fine structure analysis. Returning to our original HAADF-STEM imaging conditions, we carried out peak finding to identify atom positions followed by fitting of peaks to two-dimensional Gaussians with an offset intensity to account for differences in local background. Figure 5 presents an intensity-based analysis for Ni_1@mpgCN$_x$. The corresponding intensity-based analysis for Cu_1@mpgCN$_x$ is shown in Figure S8. Figure 5 depicts the as-acquired HAADF-STEM image as well as the results of Gaussian fitting and final atom segmentation into two categories, accounting for bright and dimmer features. By examining the histogram of intensities (Figure 5d), the major peak in the distribution for the atoms found in the image (from a total of 2,160 atoms) is located at approximately 0.003. There is, however, a second peak at approximately 0.095, also visible in the sigmoid curve of percentiles as a flattening in the curve shape, suggesting a possible second sigmoid contribution. By separating these two intensity distributions, Figure 5b marks the bright atoms presumed to be the most likely candidates for Ni species.

The intensities appear broadly consistent with atomic number contrast, as the ratio is approximately 3.2, within the range of 3–4 for the expected dependence of the HAADF intensity to $Z^{1.6\text{-}2}$. These distributions are relatively broad and likely overlap due to atom motion and differences in defocus between different atoms in the field of view. Ultimately, this intensity analysis is consistent with our STEM-EELS observations and offers the possible advantage of a wider field-of-view. Nevertheless, the combination of techniques deployed on the Ni and Cu SACs demonstrates that spectroscopic characterization remains imperative for unambiguous species identification. The presented microscopy and spectroscopy approaches extend beyond single atom spectroscopy in atomically-thin graphene and other two-dimensional materials or in crystals and atoms that are stable under electron beam irradiation. Indeed, acceptable trade-offs in the spatial resolution, stability of the sample, and STEM-EELS signal are possible for single-atom catalyst materials. Furthermore, the detection and evaluation of impurities in catalysts with high loadings of active metal species may seem more challenging and time consuming, but the comprehensive imaging and spectroscopic approach outlined in the present study is likely to remain applicable in such scenarios. Screening an adequate number of fields of view via STEM-EELS imaging, STEM-EELS at single-atom level, and intensity analysis on HAADF-STEM images will prove beneficial for assessing the actual presence and the potential monoatomic nature of impurities. At the metal loadings reported in this work, the active metals appeared at relatively low areal density (many pixels between Ni or Cu atoms), suggesting higher metal loadings and areal densities could be readily accommodated for the detection of single-atom species. EELS is highly selective toward specific elements and is capable of discerning signals at distinct element edges at characteristic energy losses. Hence, its application in identifying impurities and distinguishing them from active species, even in the presence of high concentrations of the latter, is expected to pose no significant challenge. Finally, this work may provide new directions in the field of SACs: several research groups have begun using artificial intelligence and machine learning tools to automate the detection of single atoms in TEM.[85–87] However, as shown, the use of these tools may lead to incorrect attribution of features visible in HAADF-STEM images to the presence of single atoms, or even misidentification of impurities as monoatomic active species.

Conclusion

The assessment of the individual dispersion of active metal centers in single-atom catalysts and the discrimination of catalytic species from atomically-dispersed impurities remain a challenge in the field. To address such issues, this study integrates EELS with STEM to successfully identify individually-dispersed impurities and discriminate catalytically active Ni and Cu single atoms from them. The work demonstrates the necessity of employing a multifaceted approach for assessing the individual dispersion of active species within single-atom catalyst structures. Such integrative methodologies represent a crucial step forward in advancing the characterization tools available for analyzing

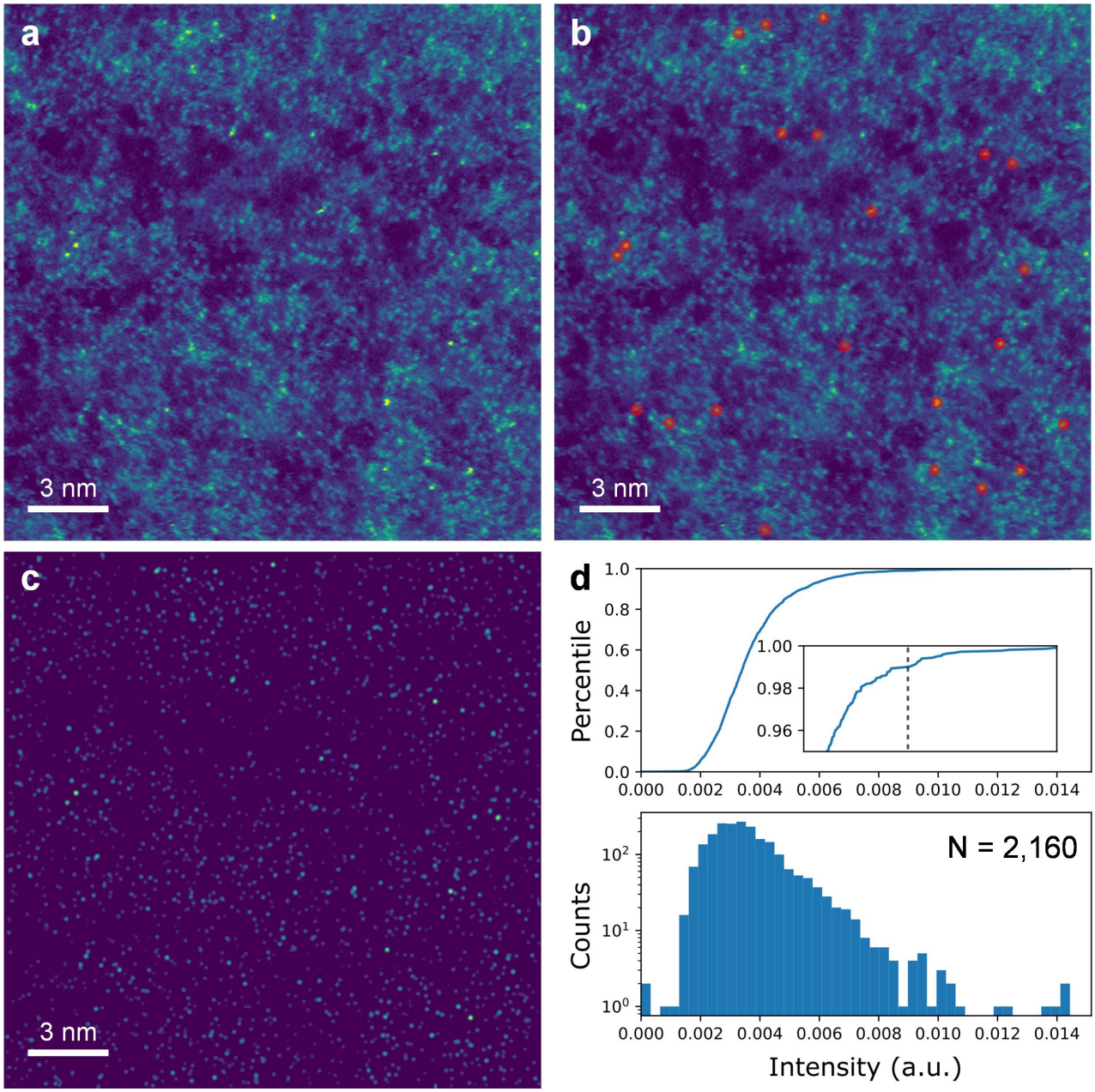

Figure 5. (a) HAADF-STEM image of Ni_1@mpgCN$_x$. (b) HAADF-STEM image annotated with automatically identified bright atoms marked. (c) Image of fitted two-dimensional Gaussian functions at all identified atom positions. (d) Intensity distribution analysis by percentile and logarithmic histogram, showing all 2,160 identified atoms in the image. The vertical dashed line in the inset (matched horizontal axes) shows the threshold used for atom segmentation in (b).

single-atom catalysts and addressing the complexities inherent in their characterization.

Acknowledgements

NA acknowledges funding from the European Commission Horizon Europe programme (grant agreement 101057430, SusPharma). GV has received funding from the European Research Council (grant agreement 101075832, SAC_2.0). SuperSTEM is the UK's National Research Facility for Advanced Electron Microscopy, funded by the Engineering and Physical Sciences Research Council (EP/W021080/1). The authors thank Dr. Giovanni Di Liberto (University of Milan-Bicocca) for the molecular models and Prof. Lorenzo Mino (University of Turin) for the support with XAS analyses.

Conflict of Interest

The authors declare no conflict of interest.

Data Availability Statement

The data that support the findings of this study are available from the corresponding author upon reasonable request.

Keywords: single-atom catalysis · catalyst characterization · catalyst impurities · STEM-EELS · atomically-resolved spectroscopy

[1] M. Kwak, J. Bok, B.-H. Lee, J. Kim, Y. Seo, S. Kim, H. Choi, W. Ko, W. Hooch Antink, C. W. Lee, G. H. Yim, H. Seung, C. Park, K.-S. Lee, D.-H. Kim, T. Hyeon, D. Yoo, *Chem. Sci.* **2022**, *13* (29), 8536–8542.

[2] M. Marchi, G. Gentile, C. Rosso, M. Melchionna, P. Fornasiero, G. Filippini, M. Prato, *ChemSusChem* **2022**, *15* (18), e202201094.

[3] L. Zhang, Y. Ren, W. Liu, A. Wang, T. Zhang, *Natl. Sci. Rev.* **2018**, *5* (5), 653–672.

[4] M. A. Bajada, J. Sanjosé-Orduna, G. Di Liberto, S. Tosoni, G. Pacchioni, T. Noël, G. Vilé, *Chem. Soc. Rev.* **2022**, *51* (10), 3898–3925.

[5] M. B. Gawande, P. Fornasiero, R. Zbořil, *ACS Catal.* **2020**, *10* (3), 2231–2259.

[6] M. Zlatar, D. Nater, D. Escalera-López, R. M. Joy, P. Pobedinskas, K. Haenen, C. Copéret, S. Cherevko, *Electrochim. Acta* **2023**, *444*, 141982.

[7] J. Liu, Y. Zou, D. Cruz, A. Savateev, M. Antonietti, G. Vilé, *ACS Appl. Mater. Interfaces.* **2021**, *13* (22), 25858–25867.

[8] M. Marchi, E. Raciti, S. M. Gali, F. Piccirilli, H. Vondracek, A. Actis, E. Salvadori, C. Rosso, A. Criado, C. D'Agostino, L. Forster, D. Lee, A. C. Foucher, R. K. Rai, D. Beljonne, E. A. Stach, M. Chiesa, R. Lazzaroni, G. Filippini, M. Prato, M. Melchionna, P. Fornasiero, *Adv. Sci.* **2023**, *10* (26), 2303781.

[9] M. Vennewald, N. M. Sackers, A. Iemhoff, I. Kappel, C. Weidenthaler, A. Meise, M. Heggen, R. E. Dunin-Borkowski, L. Keenan, R. Palkovits, *J. Catal.* **2023**, *421*, 134–144.

[10] H. Chand, A. Kumar, S. Goswami, V. Krishnan, *Fuel* **2024**, *357*, 129757.

[11] K. S. Lakhi, D.-H. Park, K. Al-Bahily, W. Cha, B. Viswanathan, J.-H. Choy, A. Vinu, *Chem. Soc. Rev.* **2017**, *46* (1), 72–101.

[12] W. Lai, Z. Miao, Y. Wang, J. Wang, S. Chou, *Adv. Energy Mater.* **2019**, *9* (43), 1900722.

[13] G. Gentile, M. Marchi, M. Melchionna, P. Fornasiero, M. Prato, G. Filippini, *Eur. J. Org. Chem.* **2022**, *2022* (37), e202200944.

[14] X. Zhao, C. Deng, D. Meng, H. Ji, C. Chen, W. Song, J. Zhao, *ACS Catal.* **2020**, *10* (24), 15178–15185.

[15] J. Zhu, P. Xiao, H. Li, S. A. C. Carabineiro, *ACS Appl. Mater. Interfaces* **2014**, *6* (19), 16449–16465.

[16] G. F. S. R. Rocha, M. A. R. da Silva, A. Rogolino, G. A. A. Diab, L. F. G. Noleto, M. Antonietti, I. F. Teixeira, *Chem. Soc. Rev.* **2023**, *52* (15), 4878–4932.

[17] Z. Chen, C. A. M. Stein, R. Qu, N. Rockstroh, S. Bartling, J. Weiß, C. Kubis, K. Junge, H. Junge, M. Beller, *ACS Catal.* **2023**, *13* (7), 4835–4841.

[18] G. Vilé, P. Sharma, M. Nachtegaal, F. Tollini, D. Moscatelli, A. Sroka-Bartnicka, O. Tomanec, M. Petr, J. Filip, I. S. Pieta, R. Zbořil, M. B. Gawande, *Solar RRL* **2021**, *5* (7), 2100176.

[19] V. Ruta, A. Sivo, L. Bonetti, M. A. Bajada, G. Vilé, *ACS Appl. Nano Mater.* **2022**, *5* (10), 14520–14528.

[20] S. Stambula, N. Gauquelin, M. Bugnet, S. Gorantla, S. Turner, S. Sun, J. Liu, G. Zhang, X. Sun, G. A. Botton, *J. Phys. Chem. C* **2014**, *118* (8), 3890–3900.

[21] K. Kim, H.-B.-R. Lee, R. W. Johnson, J. T. Tanskanen, N. Liu, M.-G. Kim, C. Pang, C. Ahn, S. F. Bent, Z. Bao, *Nat. Commun.* **2014**, *5* (1), 4781.

[22] J. Jones, H. Xiong, A. T. DeLaRiva, E. J. Peterson, H. Pham, S. R. Challa, G. Qi, S. Oh, M. H. Wiebenga, X. I. Pereira Hernández, Y. Wang, A. K. Datye, *Science* **2016**, *353* (6295), 150–154.

[23] U. Tylus, Q. Jia, K. Strickland, N. Ramaswamy, A. Serov, P. Atanassov, S. Mukerjee, *J. Phys. Chem. C* **2014**, *118* (17), 8999–9008.

[24] H. Wang, Q. Wang, Y. Cheng, K. Li, Y. Yao, Q. Zhang, C. Dong, P. Wang, U. Schwingenschlögl, W. Yang, X. X. Zhang, *Nano Lett.* **2012**, *12* (1), 141–144.

[25] T. Gan, Q. He, H. Zhang, H. Xiao, Y. Liu, Y. Zhang, X. He, H. Ji, *J. Chem. Eng.* **2020**, *389*, 124490.

[26] S. Lambert, N. Job, L. D'Souza, M. F. R. Pereira, R. Pirard, B. Heinrichs, J. L. Figueiredo, J.-P. Pirard, J. R. Regalbuto, *J. Catal.* **2009**, *261* (1), 23–33.

[27] P. Liu, Y. Zhao, R. Qin, S. Mo, G. Chen, L. Gu, D. M. Chevrier, P. Zhang, Q. Guo, D. Zang, B. Wu, G. Fu, N. Zheng, *Science* **2016**, *352* (6287), 797–800.

[28] M. J. Islam, M. Granollers Mesa, A. Osatiashtiani, J. C. Manayil, M. A. Isaacs, M. J. Taylor, S. Tsatsos, G. Kyriakou, *Appl. Catal. B* **2021**, *299*, 120652.

[29] M. Hu, Z. Wu, Z. Yao, J. Young, L. Luo, Y. Du, C. Wang, Z. Iqbal, X. Wang, *J. Catal.* **2021**, *395*, 46–53.

[30] A. C. M. Loy, S. Y. Teng, B. S. How, X. Zhang, K. W. Cheah, V. Butera, W. D. Leong, B. L. F. Chin, C. L. Yiin, M. J. Taylor, G. Kyriakou, *Prog. Energy Combust. Sci.* **2023**, *96*, 101074.

[31] L. Zhang, A. Wang, J. T. Miller, X. Liu, X. Yang, W. Wang, L. Li, Y. Huang, C.-Y. Mou, T. Zhang, *ACS Catal.* **2014**, *4* (5), 1546–1553.

[32] M.-M. Millet, G. Algara-Siller, S. Wrabetz, A. Mazheika, F. Girgsdies, D. Teschner, F. Seitz, A. Tarasov, S. V. Levchenko, R. Schlögl, E. Frei, *J. Am. Chem. Soc.* **2019**, *141* (6), 2451–2461.

[33] H. Wang, J. Shen, J. Huang, T. Xu, J. Zhu, Y. Zhu, C. Li, *Nanoscale* **2017**, *9* (43), 16817–16825.

[34] V. Muravev, G. Spezzati, Y.-Q. Su, A. Parastaev, F.-K. Chiang, A. Longo, C. Escudero, N. Kosinov, E. J. M. Hensen, *Nat. Catal.* **2021**, *4* (6), 469–478.

[35] R. Gusmão, M. Veselý, Z. Sofer, *ACS Catal.* **2020**, *10* (16), 9634–9648.

[36] K. Murugesan, A. Sagadevan, L. Peng, O. Savateev, M. Rueping, *ACS Catal.* **2023**, *13* (20), 13414–13422.

[37] J. Timoshenko, B. Roldan Cuenya, *Chem. Rev.* **2021**, *121* (2), 882–961.

[38] M. Xu, A. Li, M. Gao, W. Zhou, *J. Mater. Chem. A* **2020**, *8* (32), 16142–16165.

[39] P. Tieu, X. Yan, M. Xu, P. Christopher, X. Pan, *Small* **2021**, *17* (16), 2006482.

[40] M. M. J. Treacy, *Microsc. Microanal.* **2011**, *17* (6), 847–858.

[41] Z. Chen, S. Mitchell, E. Vorobyeva, R. K. Leary, R. Hauert, T. Furnival, Q. M. Ramasse, J. M. Thomas, P. A. Midgley, D. Dontsova, M. Antonietti, S. Pogodin, N. López, J. Pérez-Ramírez, *Adv. Funct. Mater.* **2017**, *27* (8), 1605785.

[42] E. Vorobyeva, E. Fako, Z. Chen, S. M. Collins, D. Johnstone, P. A. Midgley, R. Hauert, O. V. Safonova, G. Vilé, N. López, S. Mitchell, J. Pérez-Ramírez, *Angew. Chem. Int. Ed.* **2019**, *58* (26), 8724–8729.

[43] K. Takada, M. Morita, T. Imaoka, J. Kakinuma, K. Albrecht, K. Yamamoto, *Sci. Adv.* **2021**, *7* (32).

[44] S. Mitchell, F. Parés, D. Faust Akl, S. M. Collins, D. M. Kepaptsoglou, Q. M. Ramasse, D. Garcia-Gasulla, J. Pérez-Ramírez, N. López, *J. Am. Chem. Soc.* **2022**, *144* (18), 8018–8029.

[45] O. L. Krivanek, M. F. Chisholm, V. Nicolosi, T. J. Pennycook, G. J. Corbin, N. Dellby, M. F. Murfitt, C. S. Own, Z. S. Szilagyi, M. P. Oxley, S. T. Pantelides, S. J. Pennycook, *Nature* **2010**, *464* (7288), 571–574.
[46] W. Raza, A. B. Tesler, A. Mazare, O. Tomanec, S. Kment, P. Schmuki, *ChemCatChem* **2023**, *15* (12), e202300327.
[47] T. Furnival, R. K. Leary, E. C. Tyo, S. Vajda, Q. M. Ramasse, J. M. Thomas, P. D. Bristowe, P. A. Midgley, *Chem. Phys. Lett.* **2017**, *683*, 370–374.
[48] S. K. Kaiser, R. Lin, S. Mitchell, E. Fako, F. Krumeich, R. Hauert, O. V. Safonova, V. A. Kondratenko, E. V. Kondratenko, S. M. Collins, P. A. Midgley, N. López, J. Pérez-Ramírez, *Chem. Sci.* **2019**, *10* (2), 359–369.
[49] Q. M. Ramasse, C. R. Seabourne, D.-M. Kepaptsoglou, R. Zan, U. Bangert, A. J. Scott, *Nano Lett.* **2013**, *13* (10), 4989–4995.
[50] R. Senga, K. Suenaga, *Nat. Commun.* **2015**, *6* (1), 7943.
[51] Y. Li, W. Zhou, H. Wang, L. Xie, Y. Liang, F. Wei, J.-C. Idrobo, S. J. Pennycook, H. Dai, *Nat. Nanotechnol.* **2012**, *7* (6), 394–400.
[52] Z. Wang, J. Choi, M. Xu, X. Hao, H. Zhang, Z. Jiang, M. Zuo, J. Kim, W. Zhou, X. Meng, Q. Yu, Z. Sun, S. Wei, J. Ye, G. G. Wallace, D. L. Officer, Y. Yamauchi, *ChemSusChem* **2020**, *13* (5), 929–937.
[53] H. Jin, P. Li, P. Cui, J. Shi, W. Zhou, X. Yu, W. Song, C. Cao, *Nat. Commun.* **2022**, *13* (1), 723.
[54] T. C. Lovejoy, Q. M. Ramasse, M. Falke, A. Kaeppel, R. Terborg, R. Zan, N. Dellby, O. L. Krivanek, *Appl. Phys. Lett.* **2012**, *100* (15), 154101.
[55] J. Wang, R. You, C. Zhao, W. Zhang, W. Liu, X.-P. Fu, Y. Li, F. Zhou, X. Zheng, Q. Xu, T. Yao, C.-J. Jia, Y.-G. Wang, W. Huang, Y. Wu, *ACS Catal.* **2020**, *10* (4), 2754–2761.
[56] E. Vorobyeva, V. C. Gerken, S. Mitchell, A. Sabadell-Rendón, R. Hauert, S. Xi, A. Borgna, D. Klose, S. M. Collins, P. A. Midgley, D. M. Kepaptsoglou, Q. M. Ramasse, A. Ruiz-Ferrando, E. Fako, M. A. Ortuño, N. López, E. M. Carreira, J. Pérez-Ramírez, *ACS Catal.* **2020**, *10* (19), 11069–11080.
[57] K. E. MacArthur, T. J. A. Slater, S. J. Haigh, D. Ozkaya, P. D. Nellist, S. Lozano-Perez, *Microsc. Microanal.* **2016**, *22* (1), 71–81.
[58] R. F. Egerton, M. Watanabe, *Ultramicroscopy* **2018**, *193*, 111–117.
[59] A. Sivo, V. Ruta, V. Granata, O. Savateev, M. A. Bajada, G. Vilé, *ACS Sustainable Chem. Eng.* **2023**, *11* (13), 5284–5292.
[60] C.-Y. Wang, K. Maeda, L.-L. Chang, K.-L. Tung, C. Hu, *Carbon* **2022**, *188*, 482–491.
[61] V. W. Lau, I. Moudrakovski, T. Botari, S. Weinberger, M. B. Mesch, V. Duppel, J. Senker, V. Blum, B. V. Lotsch, *Nat. Commun.* **2016**, *7* (1), 12165.
[62] E. Vorobyeva, Z. Chen, S. Mitchell, R. K. Leary, P. Midgley, J. M. Thomas, R. Hauert, E. Fako, N. López, J. Pérez-Ramírez, *J. Mater. Chem. A* **2017**, *5* (31), 16393–16403.
[63] M. A. Bajada, G. Di Liberto, S. Tosoni, V. Ruta, L. Mino, N. Allasia, A. Sivo, G. Pacchioni, G. Vilé, *Nat. Synth.* **2023**, *2* (11), 1092–1103.
[64] M. Ullah, H. Lv, Z. Liu, X. Bai, J. Chen, Y. Zhang, J. Wang, B. Sun, L. Li, K. Shi, *Appl. Surf. Sci.* **2021**, *550*, 149368.
[65] F. Dong, Y. Li, Z. Wang, W.-K. Ho, *Appl. Surf. Sci.* **2015**, *358*, 393–403.
[66] Y. Lv, D. Ma, K. Song, S. Mao, Z. Liu, D. He, X. Zhao, T. Yao, J.-W. Shi, *J. Mater. Chem. A* **2023**, *11* (2), 800–808.
[67] B. Zhai, H. Li, G. Gao, Y. Wang, P. Niu, S. Wang, L. Li, *Adv. Funct. Mater.* **2022**, *32* (47), 2207375.
[68] Z. Jin, X. Jiang, Q. Zhang, S. Huang, L. Zhang, L. Huang, T. He, H. Zhang, T. Ohno, S. Ruan, Y.-J. Zeng, *Commun. Mater.* **2020**, *1* (1), 90.
[69] S. Pareek, M. Sharma, S. Lal, J. K. Quamara, *J. Mater. Sci. Mater. Electron.* **2018**, *29* (15), 13043–13051.
[70] J. Xu, H.-T. Wu, X. Wang, B. Xue, Y.-X. Li, Y. Cao, *Phys. Chem. Chem. Phys.* **2013**, *15* (13), 4510.
[71] H. Liu, D. Chen, Z. Wang, H. Jing, R. Zhang, *Appl. Catal. B* **2017**, *203*, 300–313.
[72] F. Fina, S. K. Callear, G. M. Carins, J. T. S. Irvine, *Chem. Mater.* **2015**, *27* (7), 2612–2618.
[73] G. Vilé, G. Di Liberto, S. Tosoni, A. Sivo, V. Ruta, M. Nachtegaal, A. H. Clark, S. Agnoli, Y. Zou, A. Savateev, M. Antonietti, G. Pacchioni, *ACS Catal.* **2022**, *12* (5), 2947–2958.
[74] M. Kottwitz, Y. Li, H. Wang, A. I. Frenkel, R. G. Nuzzo, *Chem. Methods* **2021**, *1* (6), 278–294.
[75] P. Kumar, P. Antal, X. Wang, J. Wang, D. Trivedi, O. F. Fellner, Y. A. Wu, I. Nemec, V. T. Santana, J. Kopp, P. Neugebauer, J. Hu, M. G. Kibria, S. Kumar, *Small* **2023**, *20* (15), 2304574.
[76] B. Wu, R. Yang, L. Shi, T. Lin, X. Yu, M. Huang, K. Gong, F. Sun, Z. Jiang, S. Li, L. Zhong, Y. Sun, *Chem. Commun.* **2020**, *56* (93), 14677–14680.
[77] T. Jia, D. Meng, R. Duan, H. Ji, H. Sheng, C. Chen, J. Li, W. Song, J. Zhao, *Angew. Chem. Int. Ed.* **2023**, *62* (9), e202216511.
[78] Y. Zheng, Y. Jiao, Y. Zhu, Q. Cai, A. Vasileff, L. H. Li, Y. Han, Y. Chen, S.-Z. Qiao, *J. Am. Chem. Soc.* **2017**, *139* (9), 3336–3339.
[79] Y. Li, B. Li, D. Zhang, L. Cheng, Q. Xiang, *ACS Nano* **2020**, *14* (8), 10552–10561.
[80] J. Feng, H. Gao, L. Zheng, Z. Chen, S. Zeng, C. Jiang, H. Dong, L. Liu, S. Zhang, X. Zhang, *Nat. Commun.* **2020**, *11* (1), 4341.
[81] D. Faust Akl, D. Poier, S. C. D'Angelo, T. P. Araújo, V. Tulus, O. V. Safonova, S. Mitchell, R. Marti, G. Guillén-Gosálbez, J. Pérez-Ramírez, *Green Chem.* **2022**, *24* (18), 6879–6888.
[82] J. Büker, X. Huang, J. Bitzer, W. Kleist, M. Muhler, B. Peng, *ACS Catal.* **2021**, *11* (13), 7863–7875.
[83] X. Hai, Y. Zheng, Q. Yu, N. Guo, S. Xi, X. Zhao, S. Mitchell, X. Luo, V. Tulus, M. Wang, X. Sheng, L. Ren, X. Long, J. Li, P. He, H. Lin, Y. Cui, X. Peng, J. Shi, J. Wu, C. Zhang, R. Zou, G. Guillén-Gosálbez, J. Pérez-Ramírez, M. J. Koh, Y. Zhu, J. Li, J. Lu, *Nature* **2023**, *622* (7984), 754–760.
[84] F. S. Hage, G. Radtke, D. M. Kepaptsoglou, M. Lazzeri, Q. M. Ramasse, *Science* **2020**, *367* (6482), 1124–1127.
[85] S. Mitchell, F. Parés, D. Faust Akl, S. M. Collins, D. M. Kepaptsoglou, Q. M. Ramasse, D. Garcia-Gasulla, J. Pérez-Ramírez, N. López, *J. Am. Chem. Soc.* **2022**, *144* (18), 8018–8029.
[86] K. Rossi, A. Ruiz-Ferrando, D. F. Akl, V. G. Abalos, J. Heras-Domingo, R. Graux, X. Hai, J. Lu, D. Garcia-Gasulla, N. López, J. Pérez-Ramírez, S. Mitchell, *Adv. Mater.* **2024**, *36* (5), 2307991.
[87] L. Cheng, Y. Tang, K. Ostrikov, Q. Xiang, *Angew. Chem. Int. Ed.* **2024**, *63* (5), e202313599.

Manuscript received: March 13, 2024
Accepted manuscript online: May 15, 2024
Version of record online: ■■, ■■

Research Article

Single-atom Catalysis

N. Allasia, S. M. Collins,* Q. M. Ramasse, G. Vilé* ——— **e202404883**

Hidden Impurities Generate False Positives in Single Atom Catalyst Imaging

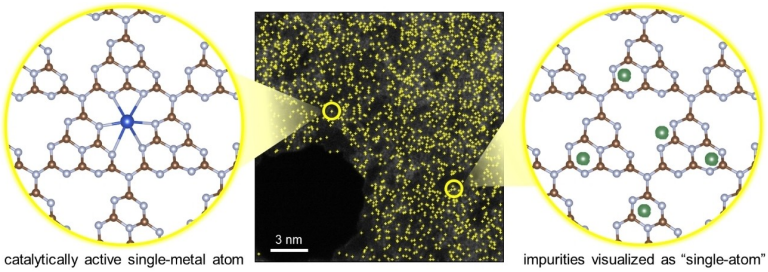

The research addresses a critical issue in the characterization of single-atom catalysts, namely the challenge of correctly identifying and distinguishing impurities and active sites at the atomic scale.